Wavelet-Based Signal Analysis of a Vehicle Crash Test

Hamid Reza Karimi
University of Agder
Department of Engineering
Faculty of Engineering and Science
N-4898 Grimstad
Norway
hamid.r.karimi@uia.no

Kjell G. Robbersmyr
University of Agder
Department of Engineering
Faculty of Engineering and Science
N-4898 Grimstad
Norway
kjell.g.robbersmyr@uia.no

Abstract: Nowadays, each newly produced car must conform to the appropriate safety standards and norms. The most direct way to observe how a car behaves during a collision and to assess its crashworthiness is to perform a crash test. This paper deals with the wavelet-based performance analysis of the safety barrier for use in a full-scale test. The test involves a vehicle, a Ford Fiesta, which strikes the safety barrier at a prescribed angle and speed. The vehicle speed before the collision was measured. Vehicle accelerations in three directions at the centre of gravity were measured during the collision. The yaw rate was measured with a gyro meter. Using normal speed and high-speed video cameras, the behavior of the safety barrier and the test vehicle during the collision was recorded. Based upon the results obtained, the tested safety barrier, has proved to satisfy the requirements for an impact severity level. By taking into account the Haar wavelets, the property of integral operational matrix is utilized to find an algebraic representation form for calculate of wavelet coefficients of acceleration signals. It is shown that Haar wavelets can construct the acceleration signals well.

Key–Words: Haar wavelet, signal analysis, vehicle crash, safety barrier

1 Introduction

Worldwide significant efforts have been made to improve the protection of vulnerable road users against injuries and deaths, especially for pedestrians. However, the situation of pedestrian safety is still severe and worrying. On the average, in China, a pedestrian is injured in every 5 min and one is killed in every 17 min. Even in a country where the traffic management is comparatively well organized, for example, the US, pedestrian safety is also the focus of public safety. In 1999 in the US, there were 4907 pedestrian killed, weighting 12% of all traffic fatalities. While the age and state of health of the pedestrian, the nature of the impact and the vehicle shape all affect the outcome of injury, the prime factor in injury/fatality risk is the vehicle impact speed [12]. Nowadays, each newly produced car must conform to the appropriate safety standards and norms. The most direct way to observe how a car behaves during a collision and to assess its crashworthiness is to perform a crash test. One needs to carry out such a test separately for each different accidents circumstances (e.g. vehicle-to vehicle collision, an offset collision, vehicle-to-barrier collision). Also, acceleration measuring devices, the data acquisition and processing have main roles in this application. This makes the testing procedure complex, time-consuming and extremely expensive. Therefore it is desirable to find a way to replace it by a computer simulation.

Occupant safety during a crash is an important consideration in the design of automobiles. The crash performance of an automobile largely depends on the ability of its structure to absorb the kinetic energy and to maintain the integrity of the occupant compartment. To verify the crash performance of automobiles, extensive testing as well as analysis are needed during the early stages of design [7].

In the last ten years, emphasis on the use of analytical tools in design and crash performance has increased as a result of the rising cost of building prototypes and the shortening of product development cycles. Currently, lumped parameter modeling (LPM) and finite element modeling (FEM) are the most popular analytical tools in modeling the crash performance of an automobile ([1], [2]). The first successful lumped parameter model for the frontal crash of an automobile was developed by Kamal in [14]. In a typical lumped parameter model, used for a frontal crash, the vehicle can be represented as a combination of masses, springs and dampers. The dynamic relationships among the lumped parameters are established using Newton's laws of motion and then the set of differential equations are solved using numerical

integration techniques. The major advantage of this technique is the simplicity of modeling and the low demand on computer resources. The problem with this method is obtaining the values for the lumped parameters, e.g. mass, stiffness, and damping. The current approach is to crush the structural components using a static crusher to get force deflection characteristics. The mass is lumped based on the experience and judgment of the analyst. Usually complicated fixtures and additional parts are attached to the component being tested to achieve the proper end conditions. This adds complexity and cost to the component crush test. Since the early 60s, the finite element method (FEM) has been used extensively for linear stress, deflection and vibration analysis. However, its use in crashworthiness analysis was very limited until a few years ago. The availability of general purpose crash simulation codes like DYNA3D and PAM-CRASH, an increased understanding of the plasticity behavior of sheet metal, and increased availability of the computer resources have increased the use of finite element technique in crash simulation during the last few years [10]. The major advantage of an FEM model is its capability to represent geometrical and material details of the structure. The major disadvantage of FE models is cost and time. To obtain good correlation of an FEM stimulation with test measurements, extensive representation of the major mechanisms in the crash event is required. This increases costs and the time required for modeling and analysis.

On the other hand, wavelet transform as a new technique for time domain simulations based on the time-frequency localization, or multiresolution property, has been developed into a more and more complete system and found great success in practical engineering problems, such as signal processing, pattern recognition and computational graphics ([13], [8]). Recently, some of the attempts are made in solving surface integral equations, improving the finite difference time domain method, solving linear differential equations and nonlinear partial differential equations and modeling nonlinear semiconductor devices ([9], [11], [15]-[21]). The approximation of general continuous functions by wavelets is very useful for system modeling and identification. Recently, the paper [23] studied the spectral decomposition and the adaptive analysis of data coming from car crash simulations. The mathematical ingredient of the proposed signal processing technique is the flexible Gabor-wavelet transform or the α-transform that reliably detects both high and low frequency components of such complicated short-time signals.

The present work intends to, emphasizing the advantages of wavelets, analyze performance of the safety barrier for use in a full-scale test. Also in this article, we use the Haar wavelets to calculate wavelet coefficients. The test involves a vehicle, a Ford Fiesta, which strikes the safety barrier at a prescribed angle and speed. The vehicle speed before the collision was measured. Vehicle accelerations in three directions at the centre of gravity were measured during the collision. The yaw rate was measured with a gyro meter. Using normal speed and high-speed video cameras, the behavior of the safety barrier and the test vehicle during the collision was recorded. Based upon the results obtained, the tested safety barrier, has proved to satisfy the requirements for an impact severity level. By taking into account the Haar wavelets, the property of integral operational matrix is utilized to find an algebraic representation form for calculate of wavelet coefficients of acceleration signals. It is shown that Haar wavelets can construct the acceleration signals well.

2 Orthogonal families of Wavelets

Wavelets are a relatively new mathematical concept, introduced at the end of the 1980s ([5]-[6], [22]). Two functions, the mother scaling function, ϕ , and the mother wavelet, ψ , characterize each orthogonal family. These are defined by the following recursive relations

$$\phi(x) = \sqrt{2} \sum_{j=-m}^{m} h_j \phi(2x - j), \tag{1}$$

$$\psi(x) = \sqrt{2} \sum_{j=-m}^{m} g_j \phi(2x - j). \tag{2}$$

where h_j and g_j are the filters that characterize the family of degree m . These filters must satisfy orthogonality and symmetry relations. Due to the choice of the filters h_j and g_j , the dilations and translations of the mother scaling function, $\phi_k^j(x)$, and the mother wavelet, $\psi_k^j(x)$, form an orthogonal basis of $L^2(R)$. This property has an important consequence: any continuous function, $f(x)$ can be uniquely projected in this orthogonal basis and expressed as, for example, a linear combination of functions ψ_k^j.

$$f(x) = \sum_{j \in Z} \sum_{k \in Z} d_k^j \psi_k^j(x)\,. \tag{3}$$

where $d_k^j = \int_{-\infty}^{\infty} f(x)\psi_k^j(x)dx$.

2.1 Haar Wavelet

The oldest and most basic of the wavelet systems is named *Haar wavelets* ([19]) which is a group of square waves with magnitudes of ± 1 in certain intervals and zero elsewhere and the normalized scaling

function is also defined as $\phi(t) = 1$ for $0 \leq t < 1$ and zero elsewhere. Just these zeros make the Haar transform faster than other square functions such as Walsh function ([3]). We can easily see that the $\phi(.)$ and $\psi(.)$ are compactly supported, they give a local description, at different scales *j*, of the considered function.

The wavelet series representation of the one-dimensional function $y(t)$ in terms of an orthonormal basis in the interval $[0, 1)$ is given by

$$y(t) = \sum_{i=0}^{\infty} a_i \, \psi_i(t) \tag{4}$$

where $\psi_i(t) = \psi(2^j t - k)$ for $i \geq 1$ and we write $i = 2^j + k$ for $j \geq 0$ and $0 \leq k < 2^j$ and also defined $\psi_0(t) = \phi(t)$. Since it is not realistic to use an infinite number of wavelets to represent the function $y(t)$, (4) will be terminated at finite terms and we consider the following wavelet representation $\hat{y}(t)$ of the function $y(t)$:

$$\hat{y}(t) = \sum_{i=0}^{m-1} a_i \, \psi_i(t) := a^T \Psi_m(t) \tag{5}$$

where $a := [a_0, a_1, \ldots, a_{m-1}]^T$, $\Psi_m := [\psi_0, \psi_1, \ldots, \psi_{m-1}]^T$ for $m = 2^j$ and the Haar coefficients a_i are determined as

$$a_i = 2^j \int_0^1 y(t) \, \psi_i(t) \, dt. \tag{6}$$

The approximation error $\Xi_y(m) := y(t) - \hat{y}(t)$ depends on the resolution *m*. Generally, the matrix H_m can be represented as

$$H_m := [\Psi_m(t_0), \Psi_m(t_1), \ldots, \Psi_m(t_{m-1})], \tag{7}$$

where $\frac{i}{m} \leq t_i < \frac{i+1}{m}$ and using (5), we get

$$[\hat{y}(t_0), \hat{y}(t_1), \ldots, \hat{y}(t_{m-1})] = a^T H_m. \tag{8}$$

For further information see the references [3]-[4], [19]-[21].

2.2 Integral Operation Matrix

In the wavelet analysis of dynamical systems, we consider a continuous operator $\tilde{O}$ on the $L_2(\Re)$, then the corresponding discretized operator in the wavelet domain at resolution *m* is defined as ([19])

$$\tilde{O}^m = T_m \, \tilde{O} \, T_m \tag{9}$$

where T_m is the projection operator on a wavelet basis of proposed resolution. Hence to apply $\tilde{O}^m$ to a function $y(t)$ means that the result is an approximation (in the multiresolution meaning) of $\tilde{O}\, y(t)$ and it holds that

$$\lim_{m \to \infty} \| \tilde{O}^m y - \tilde{O}\, y \|_2 = 0, \tag{10}$$

where the operator $\tilde{O}^m$ can be represented by a matrix P_m.

In this paper, the operator $\tilde{O}$ is considered as integration, so the corresponding matrix

$$P_m = < \int_0^t \Psi_m(\tau) \, d\tau, \Psi_m(t) >$$

$$= \int_0^1 \int_0^t \Psi_m(\tau) \, d\tau \, \Psi_m^T(t) \, dt$$

represents the integral operator for wavelets on the interval at the resolution *m*. Hence the wavelet integral operational matrix P_m is obtained by

$$\int_0^t \Psi_m(\tau) \, d\tau = P_m \Psi_m(t). \tag{11}$$

For Haar functions, the square matrix P_m satisfies a recursive formula ([3], [19]-[21]).

3 Vehicle kinematics in a fixed barrier impact

Having the acceleration measurements in three directions (x - longitudinal, y - lateral and z - vertical) by their integration we obtain corresponding velocities and displacements. Since the car undergoes the most severe deformation in the longitudinal direction, we analyze only its acceleration changes along x - axis. Integration process yields velocity and displacement in that direction. Our aim was to create a model which simulated will give the displacement curve as similar as possible to the real car's crush.

Let us remind the basic kinematic relationships between body's acceleration, velocity and displacement. The first and second integrals of the vehicle deceleration, $a(t)$, are shown below. The initial velocity and initial displacements of the vehicle are v_0 and x_0, respectively.

$$a = \frac{dv}{dt}$$

$$dv = a \, dt$$

$$\int_{v_0}^{v} dv = \int_0^t a \, dt$$

$$v = v_0 + \int_0^t a \, dt$$

(12)

$$x = x_0 + \int_0^t \left(v_0 + \int_0^t a\, dt \right) dt, \qquad (13)$$

Major parameters which characterize car's behavior during a crash are:

- maximum dynamic crush C - the highest value of car's deformation
- time at maximum dynamic crush t_m - the time when it occurs
- time of rebound velocity (or separation velocity) t_r - the time at which the velocity after the rebound reaches its maximum value.

Typical shapes of acceleration, velocity and displacement are shown in fig:curves.

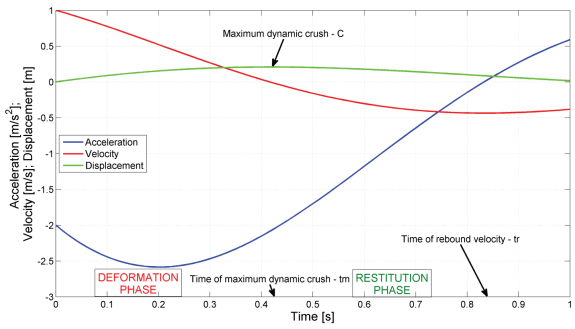

Figure 1: *Exemplary signals.*

At t_m - the time when the relative approach velocity is zero, the maximum dynamic crush occurs. The relative velocity in the rebound phase then increases negatively up to the final separation (or rebound) velocity, at which time the two masses separate from each other (or a vehicle rebounds from the barrier). At the separation time, there is no more restitution impulse acting on the masses, therefore, the relative acceleration at the separation time is zero. In another words: in the deformation phase (up to t_m) car's crush increases and during restitution phase (after t_m) it decreases to some steady value. Plots shown in fig:curves do not come from any real crash test - they are results of simulation of second order oscillating element and are provided here to graphically present dependences described above.

In the fixed barrier test, vehicle speed is reduced (velocity decreases) by the structural collapse, therefore, the vehicle experiences a deceleration in the forward direction. To study the effect of vehicle deceleration on occupant-restraint performance in a real test, the performance of the safety barrier was determined by performing a full-scale test at Lista Airport ([24]). The test involves a vehicle, a Ford Fiesta, which strikes the safety barrier at a prescribed angle and speed. The vehicle speed before the collision was measured. Vehicle accelerations in three directions at the centre of gravity were measured during the collisison. The yaw rate was measured with a gyro meter. Using normal speed and high-speed video cameras, the behaviour of the safety barrier and the test vehicle during the collision was recorded.

3.1 Test procedure

This vehicle to pole collision was performed at Lista Airport (Farsund, Norway) in 2004. A test vehicle was subjected to impact with a vertical, rigid cylinder. During the test, the acceleration was measured in three directions (longitudinal, lateral and vertical) together with the yaw rate from the center of gravity of the car. The acceleration field was 100 meter long and had two anchored parallel pipelines. The pipelines have a clearance of 5 mm to the front wheel tires. The force to accelerate the test vehicle was generated using a truck and a tackle. The release mechanism was placed 2 m before the end of the pipelines and the distance from there to the test item was 6.5 m. The vehicle was steered using the pipelines that were bolted to the concrete runaway. Experiment's scheme is shown in fig:runaway.

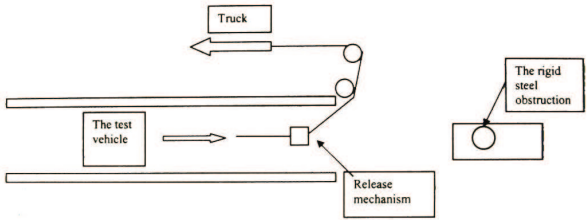

Figure 2: Scheme of the crash test.

3.2 Vehicle dimensions

Figure 1 shows the characteristic parameters of the vehicle, and these parameters are listed in Table 1.

Table 1: Vehicle dimensions in [m].

Width	Length	Height
1.58	3.56	1.36
Wheel track	Wheel base	Frontal overhang
1.42	2.28	0.63
Rear overhang		
0.65		

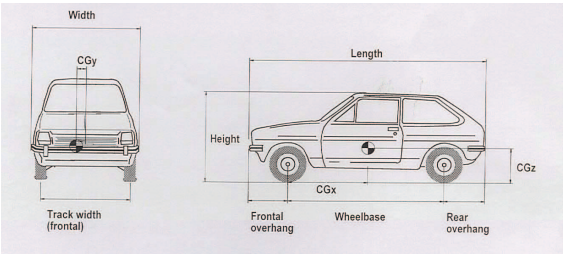

Figure 3: Vehicle dimensions.

3.3 The position of the center of gravity

To determine the position of the center of gravity each test vehicle was first weighed in a horizontal position using 4 load cells. Then the vehicle was tilted by lifting the front of the vehicle. In both positions the following parameters were recorded:

- m_1 : wheel load, front left
- m_2: wheel load, front right
- m_3 : wheel load, rear left
- m_4 : wheel load, rear right
- m_v : total load
- θ : tilted angle
- l : wheel base
- d : distance across the median plane between the vertical slings from the lift brackets at the wheel centers and the load cells.

The horizontal distance between the center of gravity and the front axle centerline, i.e. Longitudinal location, is defined as follows:

$$CG_X = (\frac{m_3 + m_4}{m_v})l$$

and Laterally location is the horizontal distance between the longitudinal median plane of the vehicle and the center of gravity (positive to the left) which is defined as

$$CG_Y = (\frac{m_1 + m_3 - (m_2 + m_4)}{m_v})\frac{d}{2}$$

Also, location of the center of gravity above a plane through the wheel centers is

$$CG_Z = (\frac{m_1 + m_2 - m_f)}{m_v\, tan\theta})l$$

where

- m_f : front mass in tilted position
- m_b : rear mass in tilted position

Table 2. shows the measured parameters to calculate the center of gravity. The position of the centre of gravity for the test vehicle is measured and the result is listed in Table 3.

Table 2: Measured parameters.

m_1 [kg]	m_2 [kg]	m_3 [kg]	m_4 [kg]	m_v [kg]
235	245	182	157	819
m_f [kg]	m_b [kg]	d [m]	l [m]	θ [deg]
443	376	1.71	2.28	22.7

Table 3: The position of the centre of gravity.

Longitudinal location $CG_X[m]$	Lateral location $CG_Y[m]$	Height $CG_Z[m]$
0.94	0.02	0.50

4 Instrumentation

During the test, the following data should be determined:

- Acceleration in three directions during and after the impact

- Velocity 6 m before the impact point

The damage should be visualized by means of:

- Still pictures
- High speed video film

The observations should establish the base for a performance evaluation. Eight video cameras were used for documentation purposes. These cameras are placed relative to the test item. Two 3-D accelerometers were mounted on a steel bracket close to the vehicles centre of gravity. This bracket is fastened by screws to the vehicle chassis. The accelerometer from which the measurements are recorded is a piezoresistive triaxial sensor with accelerometer range: $\pm 1500g$. The yaw rate was measured with a gyro instrument with which it is possible to record $1^o/msec$. Figures 2-4 show the measurements of the 3-D accelerometer in $x-$,$y-$ and $z-$ directions.

Data from the sensors was fed to an eight channel data logger. The logger has a sampling rate of 10 kHz. The memory is able to store 6,5 sec of data per channel. The impact velocity of the test vehicle was measured with an equipment using two infrared beams. The equipment is produced by Alge Timing and is using Timer S4 and photo cell RL S1c. On the test vehicle a plate with a vertical egde was mounted on the left side of the front bumper. This vertical egde will cut the reflected infrared beams in the timing equipment and thereby give signals for calculation of the speed.

The test vehicle was steered using a guide bolt which followed a guide track in the concrete runway. About $7m$ before the test vehicle hit the test item the guide bolt was released. Vehicle accelerations at the centre of gravity was measured, and also the yaw rate of the vehicle. These measurements make it possible to calculate the Acceleration Severity Index (ASI), the Theoretical Head Impact Velocity (THIV), the Post-impact Head Deceleration (PHD) value and the yaw rate. The impact speed of the test vehicle was determined. The ASI-, the THIV- and the PHD-values are calculated according to EN 1317-1 clause 6 and clause 7, and the results are shown in Table 4. Using normal speed- and high-speed video cameras, the behavior of the safety barrier and test vehicle during the collision was recorded, see Figures 5-6. The value of ASI corresponds to the requirement for impact severity level B. The THIV- and PHD-values are below the limiting values.

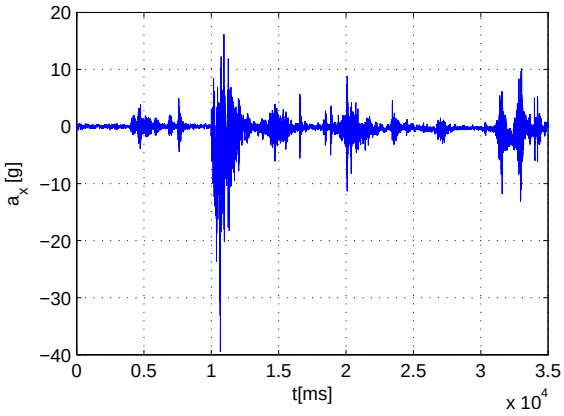

Figure 4: Acceleration signal in x- direction.

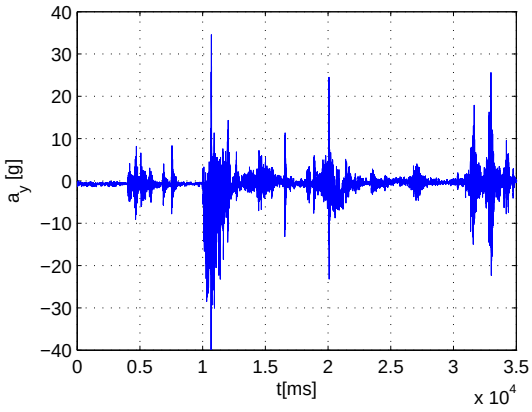

Figure 5: Acceleration signal in y- direction.

5 Wavelet-Based Signal Analysis

This section attempts to show the effectiveness of the wavelet technique to represent the measured signals of the test. By choosing the resolution level j = 7 (or $m = 2^7$) and expansion of the acceleration signal $x(t), v(t), a(t)$ in (12)-(13) by Haar wavelets, we have

$$x(t) = X\Psi_m(t)$$

$$v(t) = V\Psi_m(t)$$

and

$$a(t) = A\Psi_m(t),$$

Table 4: The calculation results.

ASI	THIV	PHD
1.28	29.9	7.8

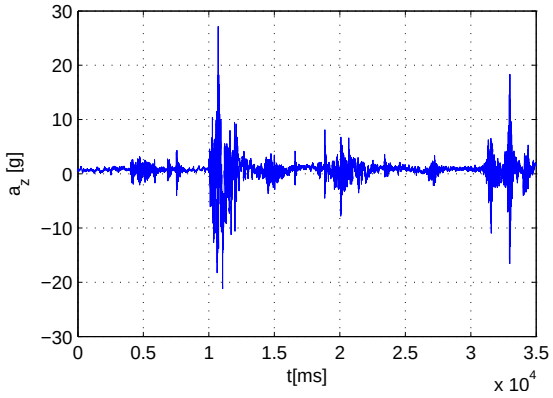

Figure 6: Acceleration signal in z- direction.

Figure 7: The situation recorded at the first contact.

in which the row vectors $X, V, A \in \Re^{1\times m}$ are the Haar wavelet coefficient vectors. Utilizing the property of the Haar integral operation matrix, Haar wavelet representation of equations (12)-(13) are, respectively,

$$V\Psi_m(t) = V_0\Psi_m(t) + \int_0^t A\Psi_m(\tau)\,d\tau$$
$$= V_0\Psi_m(t) + AP_m\Psi_m(t) \qquad (14)$$

and

$$X\Psi_m(t) =$$
$$X_0\Psi_m(t) + \int_0^t V_0\Psi_m(\tau)d\tau + \int_0^t\int_0^t A\Psi_m(\tau)\,d\tau\,dt,$$
$$= X_0\Psi_m(t) + V_0P_m\Psi_m(t) + AP_m^2\Psi_m(t) \qquad (15)$$

Constituting the Haar wavelet properties in (14)-(15), a seven-level wavelet decomposition of the measured x-acceleration signal (a_x) is performed and the

Figure 8: The situation recorded 0.148 sec after the impact.

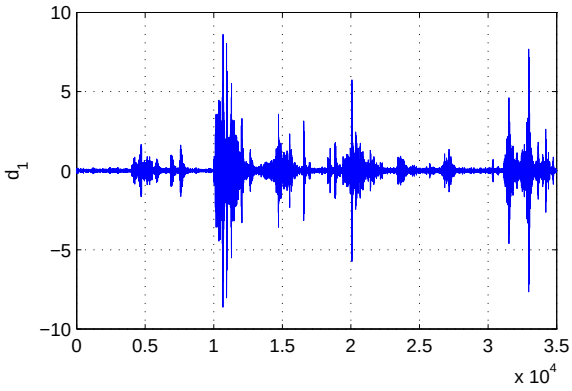

Figure 9: Detail d_1 of the 7-level Haar wavelet decomposition.

results, i.e. the approximation signal (a_7) and the detail signals (d_1-d_7) at the resolution level 7, are depicted in Figures 7-14. One advantage of using these multilevel decomposition is that we can zoom in easily on any part of the signals and examine it in greater detail. Using the approximation signal (a_1) and the detail signal (d_1) at the resolution level 1 by Haar wavelets, Figure 15 compares the constructed signal $a_x(t)$ (solid line) with the real signal (dashed line). It is noted that the approximation error between those curves in Figure 15 is decreasing when the resolution level j increases. The results in Figures 7-15 show the capability of the Haar wavelets to reconstruct the measured signals well.

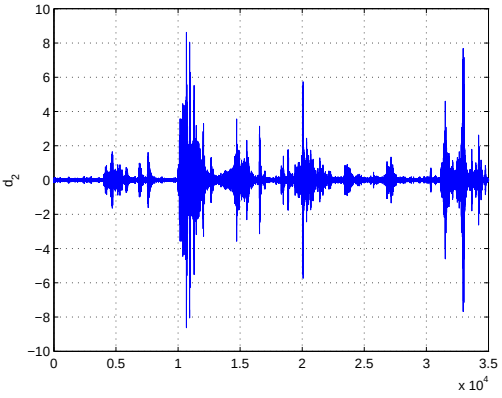

Figure 10: Detail d_2 of the 7-level Haar wavelet decomposition.

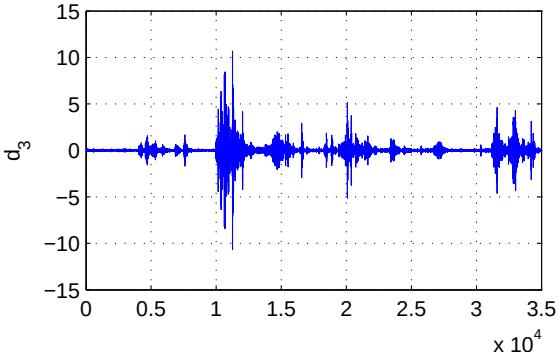

Figure 11: Detail d_3 of the 7-level Haar wavelet decomposition.

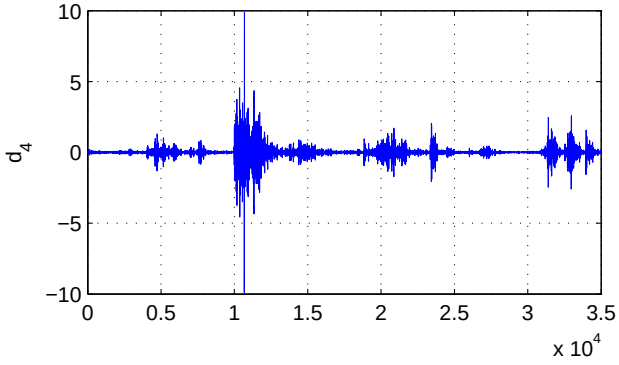

Figure 12: Detail d_4 of the 7-level Haar wavelet decomposition.

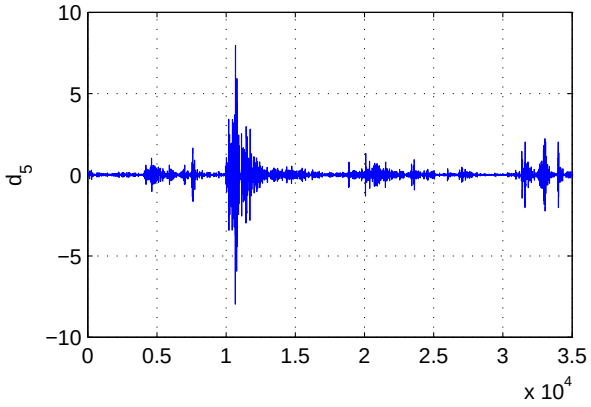

Figure 13: Detail d_5 of the 7-level Haar wavelet decomposition.

6 Conclusions

This paper studied the wavelet-based performance analysis of the safety barrier for use in a full-scale test. The test involves a vehicle, a Ford Fiesta, which strikes the safety barrier at a prescribed angle and speed. The vehicle speed before the collision was measured. Vehicle accelerations in three directions at the centre of gravity were measured during the collision. The yaw rate was measured with a gyro meter. Using normal speed and high-speed video cameras, the behavior of the safety barrier and the test vehicle during the collision was recorded. Based upon the results obtained, the tested safety barrier, has proved to satisfy the requirements for an impact severity level. By taking into account the Haar wavelets, the property of integral operational matrix was utilized to find an algebraic representation form for calculate of wavelet coefficients of acceleration signals. It was shown that Haar wavelets can construct the acceleration signals well.

References:

[1] Belytschko, T., 'On computational methods for crashworthiness', *Computers and Structure*, 1992.

[2] Borovinsek, M., Vesenjak, M., Ulbin, M., Ren, Z., 'Simulation of crash test for high containment level of road safety barriers', *Engineering Failure Analysis*, 14(8), 1711-1718, December 2007.

[3] Chen C.F. and Hsiao C.H., 'Haar wavelet method for solving lumped and distributed–parameter systems', *IEE Proc. Control Theory Appl.*, **144**, 87–94, 1997.

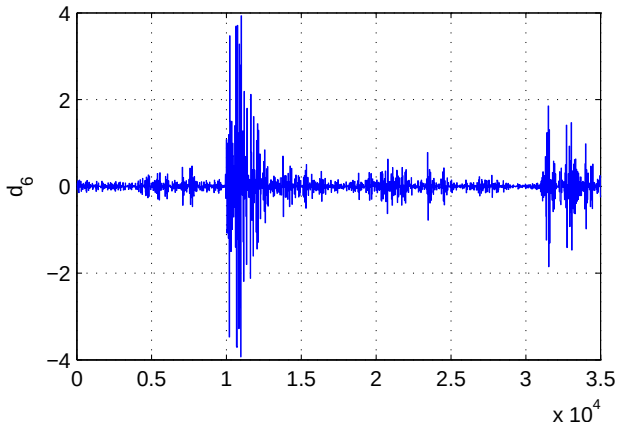

Figure 14: Detail d_6 of the 7-level Haar wavelet decomposition.

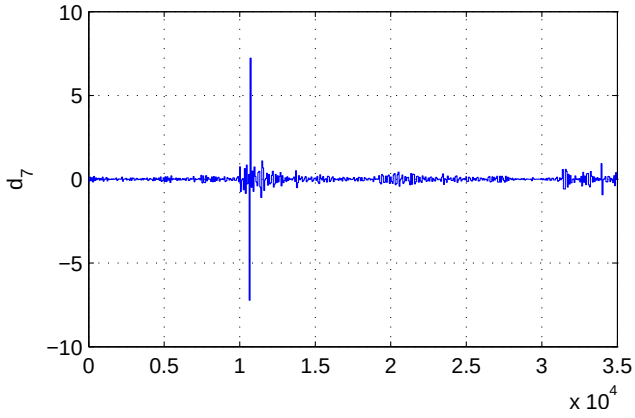

Figure 15: Detail d_7 of the 7-level Haar wavelet decomposition.

[4] Chen C.F. and Hsiao C.H., 'A state–space approach to Walsh series solution of linear systems', *Int. J. System Sci.*, **6** , 833–858, 1965.

[5] Daubechies, I.,rthogonal Bases of Compactly Supported Wavelets, *Commun. Pure Appl. Math.* , **41**, 225, 1988.

[6] Daubechies, I., *Ten Lectures on Wavelets*, SIAM, Philadelphia, 1992.

[7] Gandhi U.N. and Hu S.J., 'Data-based approach in modeling automobile crash' *Int. J. Impact Engineering*, 16(1), 95-118, 1995.

[8] Graps, A., Introduction to Wavelets, *IEEE Comput. Sci. Eng.* ,**2**, 50, 1995.

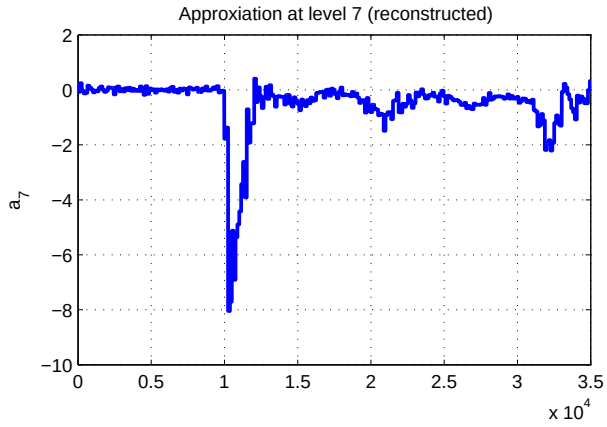

Figure 16: The approximation signal a_7 of the Haar wavelet decomposition at the resolution level 7.

[9] Griebel, M., and F. Koster, *Adaptive Wavelet Solvers for the Unsteady Incompressible Navier-Stokes Equations*, Preprint No. 669, Univ. of Bonn, Bonn, Germany, 2000.

[10] Hallquist J. and Benson D., 'DYNA3D–an explicit finite element program for impact calculations. Crashworthiness and Occupant Protection in Transportation Systems', *The Winter Annual Meeting of ASME*, San Francisco, California, 1989.

[11] Holmstron, M., Solving Hyperbolic PDEs Using Interpolating Wavelets, *J. Sci. Comput.* , **21**, 405, 1999.

[12] Huang M., *Vehicle Crash Mechanics*. Boca Raton, CRC Press, 2002.

[13] Jawerth, B., and W. Sweldens, An overview of wavelet based multiresolution analyses, *SIAM Re.* , **36**, 377, 1994.

[14] Kamal M., *Analysis and simulation of vehicle to barrier impact*. SAE 700414, 1970.

[15] Karimi H.R., Lohmann B., Moshiri B. and Maralani P.J., 'Wavelet-based identification and control design for a class of non-linear systems' *Int. J. Wavelets, Multiresoloution and Image Processing*, vol. 4, no. 1, pp. 213-226, 2006.

[16] Karimi H.R., 'A computational method to optimal control problem of time-varying state-delayed systems by Haar wavelets', *Int. J. Computer Mathematics*, **83**(2), 235–246, February 2006.

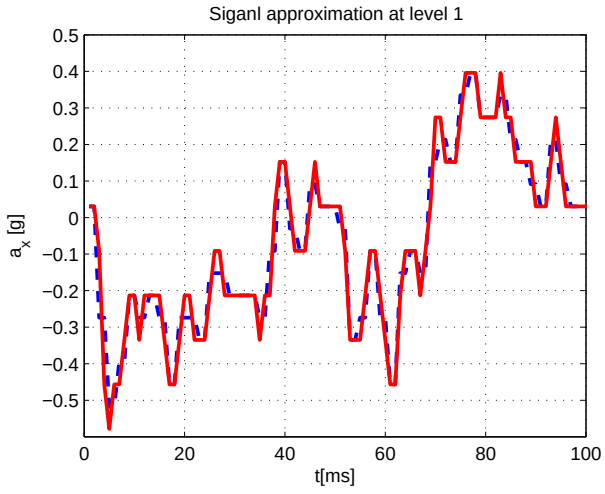

Figure 17: The constructed signal $a_x(t)$ (solid line) at the resolution level 1 with the real signal (dashed line).

[17] Karimi H.R. , 'Optimal vibration control of vehicle engine-body system using Haar functions', *Int. J. Control, Automation, and Systems*, **4**(6), 714–724, 2006.

[18] Karimi H.R. , and Lohmann B., 'Haar wavelet-based robust optimal control for vibration reduction of vehicle engine-body system', *J. of Electrical Engineering (Archiv fur Elektrotechnik)*, **89**(6), 469–478, June 2007.

[19] Karimi H.R., Lohmann B., Maralani P.J. and Moshiri B., 'A computational method for parameter estimation of linear systems using Haar wavelets', *Int. J. Computer Mathematics*, **81**(9), 1121–1132, 2004.

[20] Karimi H.R., Maralani P.J. , Moshiri B. , and Lohmann B., 'Numerically efficient approximations to the optimal control of linear singularly perturbed systems based on Haar wavelets', *Int. J. Computer Mathematics*, **82**(4), 495–507, 2005.

[21] Karimi H.R., Moshiri B., Lohmann B., and Maralani P.J., 'Haar wavelet-based approach for optimal control of second-order linear systems in time domain', *J. Dynamical and Control Systems*, **11**(2), 237–252, 2005.

[22] Mallat, S., Multiresolution Approximation and Wavelet Orthogonal Bases of $L^2(R)$, *Trans. Amer. Math. Soc.* , **315**, 69, 1989.

[23] Onchis, D.M. and Suarez Sanchez E.M., The flexible Gabor-wavelet transform for car crash signal analysis, *Int. J. of Wavelets, Multiresolution and Information Processing*, 7(4), 481-490, 2009.

[24] Robbersmyr K.G. and Bakken O.K., '*Impact test of Safety barrier, test TB 11*' Project Report 24/2001, ISSN: 0808-5544, 2001.

Appendix

Head Injury Criterion (HIC)

NHTSA (National Highway Traffic Safety Administration) proposed to determine a variable which will be one of the conditions needed to be satisfied in frontal barrier crash tests. It is defined as follows:

$$HIC = \left[\left(\frac{1}{t_2 - t_1} \int_{t_1}^{t_2} a dt \right)^{2.5} (t_2 - t_1) \right] |_{MAX}$$

where a is the effective acceleration of head in g's and $t = t_2 - t_1$ is the duration in milliseconds. The HIC, specified in the FMVSS 208 (Federal Motor Vehicle Safety Standard), states that the resultant acceleration at the center of gravity of the head of a 50th percentile male dummy must be such that the value of the HIC does not exceed 1000. t_1 and t_2 are any two points in time (milliseconds) during the crash separated by not more than a 36 ms interval [12].

Acceleration Severity Index (ASI)

The other coefficient which allows us to asses the crash severity for an occupant is an acceleration severity index (ASI). It is defined as:

$$ASI = \sqrt{\left(\frac{\overline{a_x}}{\widehat{a_x}} \right)^2 + \left(\frac{\overline{a_y}}{\widehat{a_y}} \right)^2 + \left(\frac{\overline{a_z}}{\widehat{a_z}} \right)^2}$$

where $\overline{a_x}$, $\overline{a_y}$ and $\overline{a_z}$ are the 50 - ms average component vehicle accelerations and $\widehat{a_x}$, $\widehat{a_y}$ and $\widehat{a_z}$ are corresponding threshold accelerations for each component direction. The threshold accelerations are 12 g, 9 g, and 10 g for the longitudinal (x), lateral (y), and vertical (z) directions, respectively. Since it utilizes only vehicle accelerations, the ASI inherently assumes that the occupant is continuously contacting the vehicle, which typically is achieved through the use of a seat belt. The maximum ASI value over the duration of the vehicle acceleration pulse provides a single measure of collision severity that is assumed to be proportional to occupant risk.